European Journal of Medicinal Chemistry 108 (2016) 542–552

Contents lists available at ScienceDirect

European Journal of Medicinal Chemistry

journal homepage: http://www.elsevier.com/locate/ejmech

Research paper

Drug design, synthesis, *in vitro* and *in silico* evaluation of selective monoaminoxidase B inhibitors based on 3-acetyl-2-dichlorophenyl-5-aryl-2,3-dihydro-1,3,4-oxadiazole chemical scaffold

Simona Distinto [a], Rita Meleddu [a], Matilde Yanez [b], Roberto Cirilli [c], Giulia Bianco [a], Maria Luisa Sanna [a], Antonella Arridu [a], Pietro Cossu [a], Filippo Cottiglia [a], Cristina Faggi [d], Francesco Ortuso [e, *], Stefano Alcaro [e], Elias Maccioni [a]

[a] *Dipartimento di Scienze della Vita e dell'Ambiente, Università degli Studi di Cagliari, Via Ospedale 72, 09124 Cagliari, Italy*
[b] *Facultad de Farmacia, Departamento de Farmacología, Universidad de Santiago de Compostela, Campus Vida, La Coruña, 15782 Santiago de Compostela, Spain*
[c] *Dipartimento del Farmaco, Istituto Superiore di Sanità, V.le Regina Elena 299, 00161 Rome, Italy*
[d] *Dipartimento di Chimica "Ugo Schiff", Via della Lastruccia, 3-13 - 50019 Sesto Fiorentino, Italy*
[e] *Dipartimento di Scienze della Salute, Università; "Magna Græcia" di Catanzaro, Campus "S. Venuta", Viale Europa, 88100 Catanzaro, Italy*

ARTICLE INFO

Article history:
Received 10 March 2015
Received in revised form
10 December 2015
Accepted 12 December 2015
Available online 17 December 2015

Keywords:
2,3-Dihydro-1,3,4-oxadiazoles
Neurodegenerative disorders
MAO-B
Docking
Molecular dynamics

ABSTRACT

With the aim to identify new, potent and selective monoamine oxidase B (MAO-B) inhibitors, molecular interaction field analysis has been applied to a MAO-B complex with 3-acetyl-2,5-diaryl-2,3-dihydro-1,3,4-oxadiazole chemical structure, known as a privileged scaffold for this target. Several compounds displayed potent *in vitro* activity, exhibiting IC_{50} values in the medium to low nanomolar range. The enantiomers of most promising derivatives were separated by enantioselective HPLC and *in vitro* evaluated. Experimental results, according to theoretical drug design, clearly indicated a key role of the ligand stereochemistry in the target recognition/inhibition. In particular the (*R*)- enantiomers showed the best activity with respect to the (*S*)- stereoisomer. Finally, docking experiments coupled to molecular dynamics (MD) simulations, were applied for understanding the putative MAO -B binding modes of the new compounds providing detailed information for further structural optimization.

1. Introduction

Rational design, synthesis, enantioseparation and enzymatic characterization of new 3-acetyl-2,5-diaryl-2,3-dihydro-1,3,4-oxadiazoles led to a series of novel monoamine oxidase (MAO) inhibitors [1]. MAO are ubiquitous enzymes that play a key role in the degradation of exogenous and endogenous amines. Dopamine (DA), norepinephrine (NE), epinephrine, serotonin (5HT), and 2-phenylethylamine (PEA) [2] are among the most common substrates. The mammalian family of MAOs consists of two isozymes, namely MAO-A and MAO-B, differing in their selectivity versus substrates and inhibitors, 5HT and NE are preferentially deaminated by the A isoform, whereas 2-phenylethylamine and benzylamine are MAO-B substrates [3]. Although the two isoforms share a high sequence similarity, they differ in shape and volume of the catalytic site allowing to discover selective binders. In fact, structural studies reported the presence of a single cavity of about 550 $Å^3$ for MAO-A, whereas MAO-B has a tight and longer dipartite cleft, named entrance and substrate cavities. These two pockets can merge into a single cavity of ~700 $Å^3$ [4]. Therefore, selective, potent cavity-spanning, MAO-B inhibitors have been identified such as safinamide [5,6], coumarin derivatives [7], farnesol [8], caffeine derivatives [9,10] and the anti-diabetes drug pioglitazone [11]. An increase of the DA levels as well as a neuroprotective effect can be observed following the inhibition of MAO-B [12–16] As a consequence, selective irreversible human MAO-B inhibitors (hMAO-Bi) are used alone or in combination with other drugs, in the treatment of both Parkinson's (PD) [17,18] and Alzheimer's (AD) diseases [19–22]. In fact, the increased levels of MAO-B in both PD patients and elderly population [23,24], may leads to an increased production of hydrogen peroxide and other reactive oxygen species, responsible for neuron degeneration [25–28]. Moreover, it has

* Corresponding author.
E-mail address: ortuso@unicz.it (F. Ortuso).

http://dx.doi.org/10.1016/j.ejmech.2015.12.026
0223-5234/

been proposed that the degeneration of the dopaminergic neurons, observed in PD patients could be related to the radical species overproduction deriving from an accelerated dopamine metabolism [29–31] Thus, neurological degeneration in the central nervous system (CNS) and in particular in *"substantia nigra"*, could be associated to the oxidative stress, with an increased MAO-B activity, and with a decreased elimination rate of free radical species. MAO-A expression, differently from MAO-B, does not increase with age, suggesting that a totally independent mechanism regulates the expression of the two enzymatic isoforms [32,33].

Due to the relevance of this target many classes of compounds were recently synthesized and tested for the inhibitory activity towards MAO-B [34–37]. Previously, we identified highly potent and selective MAO inhibitors 1-thiocarbamoyl-3,5-diaryl-4,5-dihydro-(1H)-pyrazole [38] and 2-thiazolylhydrazones [39,40]. Moreover, in a recent study we demonstrated that the 2,3-dihydro-1,3,4-oxadiazoles can be considered as a new interesting scaffold for MAO-B selective inhibitors [1]. In this work, extending our previous studies [36–39], we introduced a second chlorine atom on the phenyl ring. According to our binding mode models, the second chlorine atom points toward the Flavin Adenin Dinucleotide (FAD) co-factor. Docking studies highlighted the preference of the chiral carbon (R)- configuration for the binding to the MAO-B active site (Fig. 1). Hence, according to the structural indication, acquired by molecular interaction field analyses, we synthesised and tested a series of 3-acetyl-2-(3,4-dichlorophenyl)-5-aryl-2,3-dihydro-1,3,4-oxadiazoles 4a-j, in order to evaluate the influence on the biological activity of the introduction of a 3,4-dichlorophenyl moiety in the position 2 of the dihydrooxadiazole scaffold. Furthermore, given the presence of a chiral centre at the position 2 of the dihydrooxadiazole ring, the biological activity of the pure enantiomers was investigated.

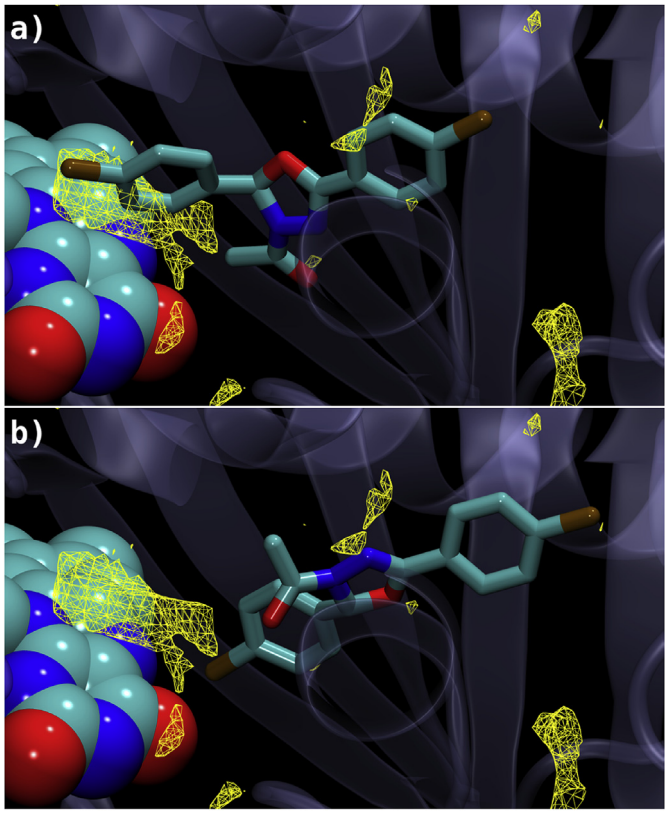

Fig. 1. Chlorine molecular interaction field (yellow wireframe grids) displayed on previous reported [1] a) P_a and b) P_b theoretical complexes. The FAD cofactor is reported in spacefill notation and the ligand in sticks cyan carbon and brown chlorine atoms coloured. The rest of the enzyme is depicted in transparent violet cartoon (For interpretation of the references to colour in this figure legend, the reader is referred to the web version of this article.)

2. Results and discussion

2.1. Design of compounds *4a-j*

Starting from previously reported theoretical complexes between MAO-B and the 2-(4-chlorophenyl)-3-acetyl-5-(4-chlorophenyl)-2,3-dihydro-1,3,4-oxadiazole [1] an extended molecular interaction fields (MIFs) analysis was carried out. After removing the inhibitor, the interaction capabilities of the MAO-B active site were investigated by means of appropriate probes (Experimental section) as implemented in the program GRID [41]. The resulting isocontour maps were inspected taking into account the two most energy stabilized previously reported poses (P_a and P_b) of the inhibitor into the hMAO-B binding cleft [1]. MIFs indicated strong interaction between the target and organic chlorine suggesting the possibility to include a second chlorine atom on the *p*-chlorophenyl ring substituent located at the position 2 of the dihydrooxadiazole ring (Fig. 1).

Bromine contribution was, successively, evaluated by means of BR probe. The visual inspection of the computed isocontour maps revealed the possibility to replace the p-chlrophenyl at 5 position moiety with the corresponding bromine analogues. In fact, taking into account the same energy threshold (Experimental section), BR map demonstrated wider surface than CL one but it did not discriminated between the two aromatic rings located at oxadiazole ring positions 2 and 5 respectively (Fig. S1). The role of other substituents was also investigated by computing the MIFs using C3 (methyl group), AR.COO (aromatic carboxylic moiety) and ON (nitro group) probes. The C3 map graphical inspection has suggested the methyl group as a possible *substituent for both aromatic rings* (Fig. S2). *The energy threshold required to overlap both* P_a and P_b poses was about 2 kcal/mol disfavoured with respect to halogen mimicking probes, so we considered the introduction of the methyl on the aromatic ring at position 5 only. A similar scenario was observed for AR.COO, even if its recognition of the aromatic ring located at oxadiazole position 5 was stronger (Fig. S3). On the other hand, considering that our target is located in the CNS, a carboxylic group was considered much too hydrophilic. As a consequence, another electron withdrawing electron withdrawing substituent, such as the nitro group, was theoretically investigated by means of the ON GRID probe (Fig. S4). Nitro group MIFs overlapped both aromatic rings. Finally, MIFs analyses interestingly highlighted a key role of the oxadiazole ring chiral centre that allowed, in (*R*)-configuration, the best superimposition between GRID maps and the ligand aromatic rings.

A requirement important for selectivity seem to be the ability of the inhibitors to fit within the elongated bipartite cavity of MAO-B, which is bigger (700 $Å^3$) and narrower than the single substrate cavity of MAO-A (550 $Å^3$) [4]. Therefore the shape of binding site was considered and the skeleton of the series was maintained because of its ability to occupy both cavities. In fact previous series showed good selectivity toward MAO-B [1,38–40,42].

2.2. Synthesis

The **4a-j** series was synthesized according to a previously described procedure [1] as illustrated in Scheme 1.

Briefly, the suspension in acetic anhydride of the appropriate benzoylhydrazide was heated under reflux until the formation of a

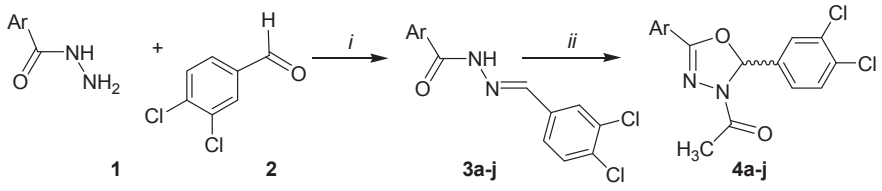

i: CH_3COOH (CAT)/ EtOH, reflux; *ii*: $(CH_3CO)_2O$, reflux

Scheme 1. Synthetic pathway to compounds **4a-j**.

yellow–orange solution was observed. The reaction mixture was then poured onto ice water and vigorously stirred. The obtained precipitate was then washed with 10% aqueous $NaHCO_3$ solution, water, and purified by crystallization. All of the products were characterised by means of both analytical and spectroscopic methods (Experimental section and Supplementary data) and tested towards MAO-A and MAO-B.

2.3. Biological activity

The inhibitory activities of compounds **4a-j** on human recombinant MAO –A and –B isoforms, expressed in baculovirus infected BTI infected cells, as IC_{50}, are reported in Table 1. Tested compounds demonstrated no interference with the measurements, since they were unable to react directly with the Amplex Red reagent. The kinetic parameters of *h*MAO-A and *h*MAO-B were evaluated in the presence of different tyramine concentrations. In our experiments, hMAO-A displayed a Michaelis constant (K_m) of 514 ± 46.8 μM and a maximum reaction velocity (V_{max}) of 301.4 ± 27.9 nmol/min/mg protein, whereas hMAO-B showed a K_m of 104.7 ± 16.3 μM and a V_{max} of 28.9 ± 6.3 nmol/min/mg protein (n = 5). Active compounds showed reversible behaviour according to the method proposed by Cer et al. [43]. Therefore, reported IC_{50} is a useful tool to determine the relative activity of the compounds within the series as well as to determine substituent and key positions in the scaffold.

Half of the tested compounds exhibited inhibitory activity towards hMAO-B at nM concentration, with the exception of compound **4b** which inhibited the corresponding MAO activity by approximately 40–50% at the concentration of 100 μM and compounds **4g** and **4i** that were inactive at 100 μM. Compounds **4a** and **4j** were effective in the μM range. Interestingly, none of the tested compounds exhibited activity towards the A isoform of the enzyme at the tested concentration of 100 μM.

2.4. Structure activity relationships

Biological tests confirmed our hypothesis, that the introduction of a 3,4-dichlorophenyl moiety in the position 5 of the dihydrooxadiazole ring could lead to more effective and selective compounds with respect to the previously reported mono-chloro derivatives (i.e. the mono-chloro analogue of **4f** was inactive on MAO-A whereas demonstrated a MAO-B IC_{50} equal to 121.62 ± 9.63 nM) [1]. Although an excellent remote Hammett correlation (σ_p or σ_p^+) has been found for *para* substitution in the two aryl rings at the positions 2 and 5 of the dihydrooxadiazole [44], the electronic effect of the substituent in the *para* position of the phenyl moiety at the position 5 of the dihydrooxadiazole did not seem to play a relevant role in determining the potency of the inhibitors. On the contrary, just the presence of a substituent in this position seemed to be essential for the activity, probably due to the need of bulky substituent in this position. This hypothesis was corroborated by the low activity exhibited by compound **4a** and **4b** bearing a pyridil and a phenyl substituent respectively. However either the introduction of a dimethylamino moiety or of a cyano as in compound **4g** and **4i**, led to a decrease of the inhibitory activity. It is worth to note that the introduction of a methyl substituent in the ortho position, as in compound **4j**, led to decrease of the inhibitory potency more than 100 fold higher than the corresponding para-substituted compound **4d**. Hence a complex blend of electronic and steric effects should be considered to determine the best substitutions for the biological activity.

Table 1
Inhibitory activities towards hMAO A and hMAO-B of 3-acetyl-2-(3,4-dichlorophenyl)-5-aryl-2,3-dihydro-1,3,4-oxadiazoles derivatives **4a-j**. Data are reported in nM.

Compound	**Ar**	hMAO-A (IC_{50})	hMAO-B (IC_{50})
4a	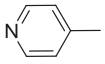	**	69360 ± 3510
4b	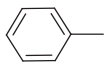	**	***
4c	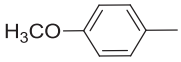	**	217.99 ± 10.62
4d	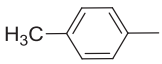	**	19.35 ± 0.68
4e	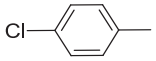	**	626.82 ± 36.52
4f	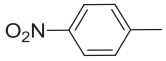	**	9.46 ± 0.57
4g	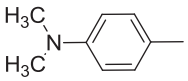	**	**
4h	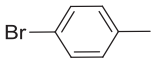	**	67.69 ± 4.27
4i	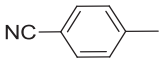	**	**
4j	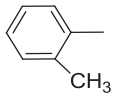	**	2460 ± 170
Clorgyline		4.60 ± 0.30	61350 ± 1130
Deprenyl		67250 ± 1020	19.00 ± 0.86
Iproniazide		6560 ± 760	7540 ± 360
Moclobemide		3613.80 ± 193.70	*

All IC_{50} values shown in this table are the mean ± S.E.M. from five experiments.
* Inactive at 1×10^6 nM (highest concentration tested).
** Inactive at 100000 nM (highest concentration tested). At higher concentration the compounds precipitate.
*** 100000 nM inhibits the corresponding MAO activity by approximately 40–45%. At higher concentration the compounds precipitate.

2.5. Enantiomeric mixture resolution

All the synthesized compounds have a stereogenic centre at the position 2 of the heterocyclic ring. **4d**, **4e** and **4f** were chosen to perform the separation of the single enantiomers and to evaluate the influence of stereochemistry on their biological properties. Repetitive semipreparative HPLC resolutions carried out on the Chiralpak IA chiral stationary phase (CSP) using the mixture dichloromethane/DEA 100/0.1 (v/v) as eluent enabled us to easily collect tens of mg of enantiopure samples (Table S1). The enantiomeric nature of the samples obtained on mg-scale was demonstrated by polarimetric (Table S1) and circular dichroism (CD) analysis (Fig. S5).

The chiroptical properties of the enantiopure antipodes were perfectly specular (Table S1 and Fig. S2). The absolute configuration of the enantiomers of **4e** and **4f** was empirically established by CD correlation method using the enantiomers of **4d** as reference samples. Crystallization of the second eluted enantiomer of (-)-**4d** (in the chromatographic conditions reported in Table S1) from ethanol/water afforded single crystals which were suitable for X-ray diffraction analysis. An Oak Ridge Thermal Ellipsoid Plot Program (ORTEP) view of (*S*)-(-)- **4d** is showed in Fig. 2. The replacement of the methyl group on the phenyl ring (compound **4d**) by a chlorine atom (compound **4e**) or a nitro group (compound **4f**) did not produce significantly alteration in the spectral location of the maximum and minimum of the representative CD bands recorded in ethanol solution (Fig. S5).

The pure enantiomers of **4e** and **4f**, respectively the less active and the most active compounds in the nM range, were then evaluated for their ability to inhibit the two different MAO isoforms. Also in this case no activity towards MAO-A at the concentration of 100 mM was observed. The results for MAO-B isoform are reported in Table 2. In agreement with molecular modelling suggestion the activity is exclusively (**4e**) or mostly (**4f**) associated with the (*R*)-enantiomer.

2.6. Molecular modelling

In order to rationalize at molecular level the enzyme inhibition of most promising compounds, suggesting their putative binding mode, docking and molecular dynamics (MD) simulations were carried out. Thus, we validated our docking protocol performing self and cross-docking of seven crystallized inhibitors, (Tables S1 and S2), into the hMAO-B crystal structure deposited into the Protein Data Bank [45] with code 2V5Z [7]. The purpose of this task was to estimate the efficiency of our docking protocol in predicting the correct orientation of original inhibitors into the substrate binding cavity. The biological activity of reference compounds

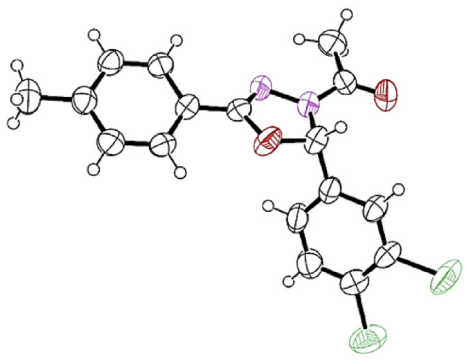

Fig. 2. An ORTEP view of the molecular structure of (*S*)-(-)-**4d**.

Table 2
Inhibitory activities towards hMAO-B of 3-acetyl-2-(3,4-dichlorophenyl)-5-aryl-2,3-dihydro-1,3,4-oxadiazoles **4e** and **4f** as pure enantiomers and racemates. Data reported in nM.

Compound	Structure	hMAO-B (IC_{50})
(±) **4e**	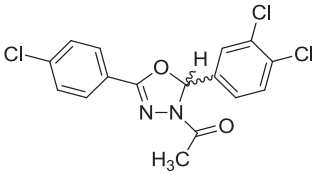	626.82 ± 36.52
(*R*)-(+) **4e**		203.59 ± 18.61
(*S*)-(-) **4e**		**
(±) **4f**	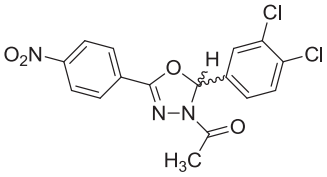	9.46 ± 0.57
(*R*)-(+) **4f**		7.61 ± 0.64
(*S*)-(-) **4f**		523.46 ± 41.30

Each IC_{50} values is the mean ± S.E.M. from five experiments.
** Inactive at 100000 nM (highest concentration tested).

varies with a Ki ranging from 35 to 0.10 μM. Among the docking settings implemented in Glide [46] software (see the Experimental section), Quantum Mechanics-polarized ligand docking (QMPL) workflow [47,48] successfully reproduced the crystallographic poses of 5 out of 7 compounds within 1.6 Å root-mean-square deviation (RMSD). However, also the docking pose of farnesol, the co-crystallized ligand reported in 2BK3 [8] PDB model, in absence of electrondensity maps could be considered good. In fact, farnesol has a plausible pose rotated of almost of 180° and the second best pose, is slightly shifted compared to experimental data even if with an RMSD value > 2 Å (Fig. 3). (Table S1).

QMPL docking workflow combines docking with *ab initio* for ligand charges calculation within the protein environment. QMPL workflow consists of three steps: in the first one protein–ligand complexes are generated with Glide (Grid Based Ligand Docking with Energetics).

In the second step, a mixed quantum mechanical/molecular mechanics (QM/MM) method is used to compute the ligand charge distribution. The protein is defined as the MM region, and the ligand is defined as the QM region. In the third step, the ligands are submitted to another Glide docking run where the ligand charges are substituted with the new charge sets calculated in the second step [47,48].

The same protocol was applied to dock the separated enantiomers (*R*)-**4e** and (*R*)-**4f**. Due to lack of accuracy of docking scores, the simple docking experiment alone is not often sufficient to rank binding scores with a linear correlation with experimentally measured binding affinities of known complexes [49]. Therefore we decided to use a combination of docking and MD. Hence, to better estimate the ligand–receptor interaction energies, the poses, reporting an RMSD >2 Å within the top five ranked binding poses, were submitted to 10 ns of MD simulations (pose [1] and [2] Table 3). Actually, explicit solvent MD, coupled with efficient free-energy sampling algorithms, can potentially offers accurate prediction of ligands to proteins binding free energies. Firstly, the molecular dynamic simulation protocol was validated considering the 7 crystal taken into account for docking validation in three possible system setting: monomer, dimer and dimer in membrane (Fig. 4).

We decided to consider the enzyme embedded into the mitochondrial membrane since in literature has been reported its key role in compound recognition. In particular, it was reported that the loop 85–112 is involved in the substrate catalytic site entrance

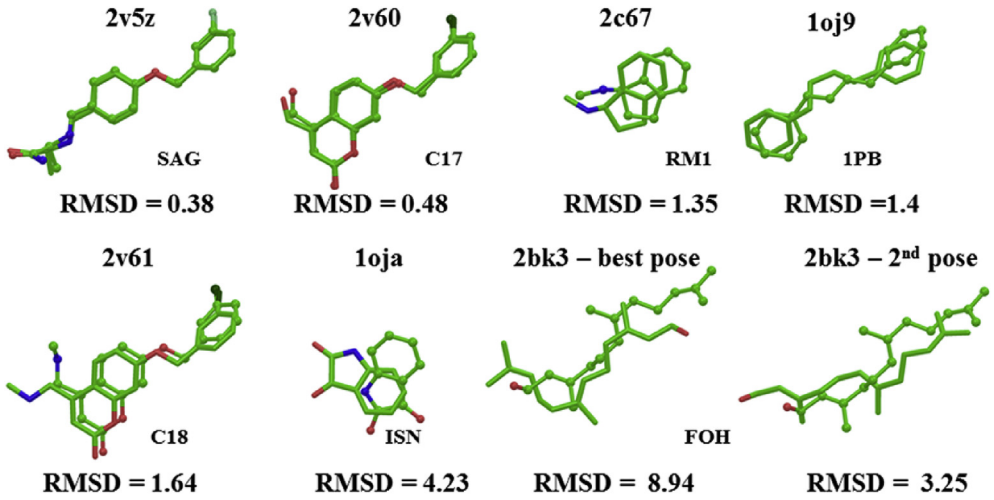

Fig. 3. Results of seven self and cross-docking experiments performed using 2V5Z as receptor model. Below each docking superimposition is reported the RMSD between co-crystallized (in ball and sticks) and first pose (in sticks). For 2BK3 ligand is reported also the second docking pose. The inhibitor ID correspondence is SAG: Safinamide; C17: 7-[(3-chlorobenzyl)oxy]-2-oxo-2H-chromene- 4-carbaldehyde; RM1: N-methyl-1(R)-aminoindan; 1 PB: 1,4-diphenyl-2-butene[(1E)-4-phenylbut-1-enyl]benzene; C18:7-[(3-chlorobenzyl)oxy]-4-[(methylamino)methyl]- 2H-chromen-2-one; ISN: isatin; FOH: farnesol.

Table 3
Averaged energies of interaction between new compounds and hMAO-B. Tot-E, Coul-E and vdW-E are respectively the total interaction energy, its electrostatic and van der Waals terms expressed in kcal/mol. The different starting poses are indicated by[1] and[2].

	Tot-E	Coul-E	vdW-E
(*R*)-4e[1]	−56.76	−5.38	−45.78
(*R*)-4e[2]	−56.19	−2.98	−51.79
(*R*)-4f[1]	−64.15	−9.26	−50.39
(*R*)-4f[2]	−63.75	−6.89	−48.12

correct prediction of the interaction energy.

Thus the monomer MD setting was used to run further simulation taking into account 2 starting poses per compound. The best pose results are illustrated in Fig. 6. Compound **4e** was able to enter deeply in the binding cavity and was stabilized by hydrophobic and aromatic interactions (Fig. 6a–c). Although the dichlorophenyl moiety was able to rotate, still the π–π interaction with Phe343 was conserved. On the contrary, compound **4f** was kept between the entrance and the catalytic cavity separated by the Ile199 due to

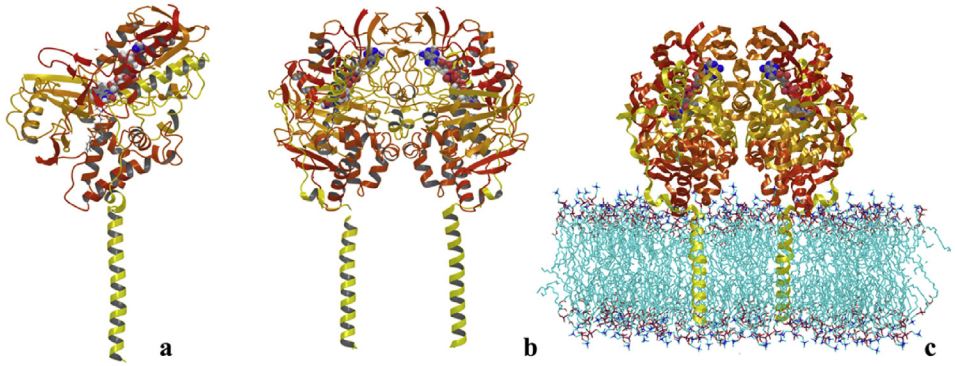

Fig. 4. Overview of MAO B a) monomer; b) homodimer; c) homodimer embedded in a lipid bilayer.

modulation [50]. We observed that the estimated interaction energies well correlate with ΔG of dissociation data with all settings (Fig. 5). However, the monomer shows the best correlation with a $r^2 = 0.89$ (0.98 if we leave the crystal 1OJA out of the evaluation).

The inhibitor ID correspondence is SAG: Safinamide; C17: 7-[(3-chlorobenzyl)oxy]-2-oxo-2H-chromene- 4-carbaldehyde; RM1: N-methyl-1(R)-aminoindan; 1 PB: 1,4-diphenyl-2-butene[(1E)-4-phenylbut-1-enyl]benzene; C18:7-[(3-chlorobenzyl)oxy]-4-[(methylamino)methyl]- 2H-chromen-2-one; ISN: isatin; FOH: farnesol.

According to these data, the presence of the membrane into the theoretical models, although relevant in the stage of compound entrance and recognition, was found to be not essential for the the interaction of the bulky nitro moiety with residues and waters in this region. More in details, compound **4f** resulted stabilized within the binding site through an array of aromatic (Tyr326, Phe168), hydrophobic (Leu171, Ile199, Leu167, Ile198), and H-bond interactions with binding site residues (Fig. 6d–f and Fig. S6).

The H-bond between the **4f** carbonyl and the hydroxyl group of the important residue Tyr435, which, together FAD and Tyr398, delimits the aromatic cage pivotal for MAO activity, was monitored and found to be stable along the whole MD simulation (Fig. S7). In addition, the number of good contacts was higher for **4f** compared to **4e** (Fig. S6). Furthermore, the averaged energy of interaction (Table 3) was in accordance with the difference of activity and underlines the higher weight of van der Waals interactions

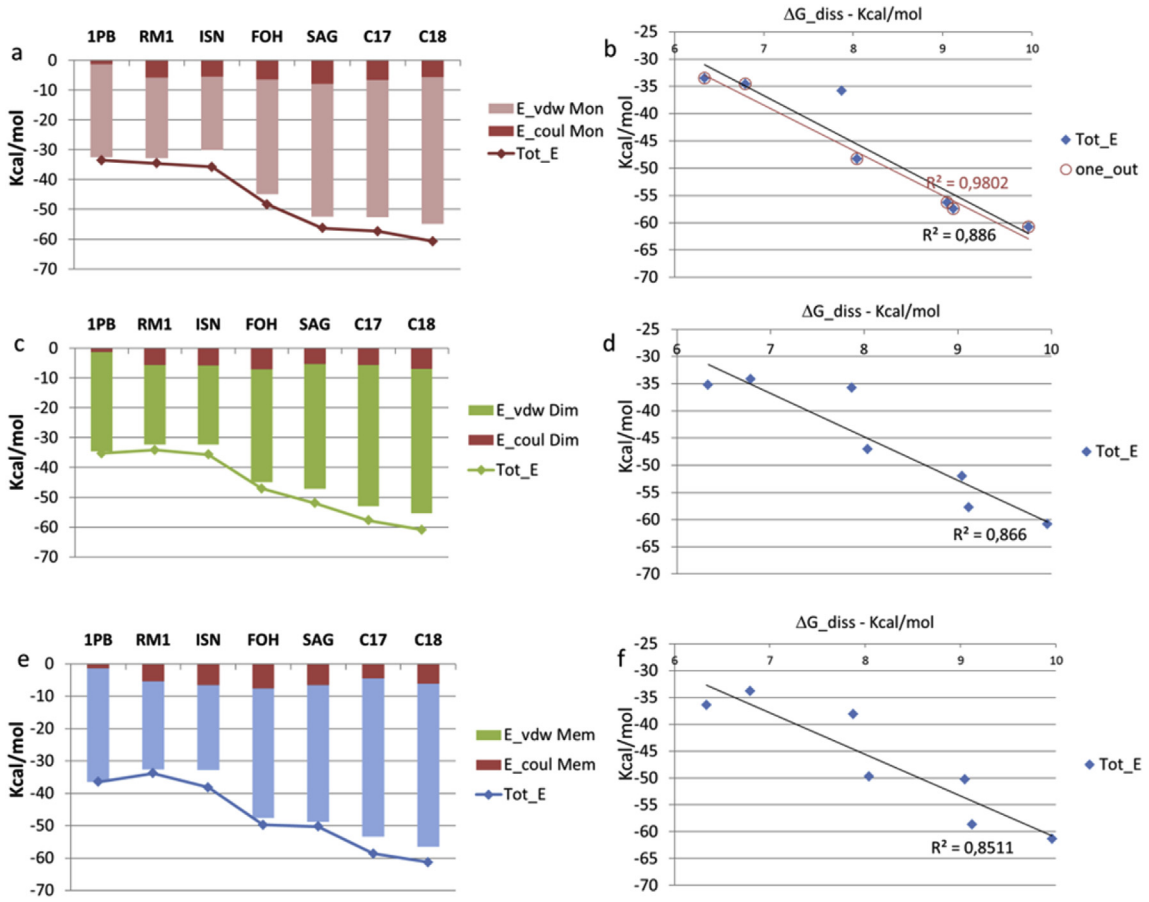

Fig. 5. MD energy analysis. Inhibitors are arranged from left to right by increasing magnitude of ΔG of dissociation. Sum of binding energy components for each inhibitor and setting (a) monomer, (c) dimer, (e) membrane. The Total energy (Tot_E) of interaction is shown with a line. Besides each histogram: figures (b), (d) and (f), the related linear regression plot and r^2 values for the sum of all interaction energies between each inhibitor and MAO B.

contribution.

With the aim to estimate the drug-likeness of the compounds, *in silico* ADME-tox prediction has been carried out [51]. Since **4f** was identified as the best inhibitor of our series, we investigated its absorption, distribution, metabolism, excretion and toxicity (ADMEtox) properties using the Qikprop [52] software. Such an approach provides molecular properties by means of a comparison of the novel compound with respect to the 95% of known drugs. The computed molecular descriptors are shown in Table S4. All properties were within the ranges specified. The predicted IC_{50} for human Ether-à-go-go-Related Gene (HERG) K + Channel Blockage was borderline in its value. However, considering the possibility of a limited error of prediction in discriminating a safe or not-safe compound, biological experiments are needed. Tissue distribution is an important element of the pharmacokinetic (PK) profile of a drug united with knowledge of the *in vitro* activity. The activity of this compound should occur in the brain, therefore we paid great attention on analysing *in silico* molecular descriptors that are required for a CNS active agent like the polar surface area (PSA) and the logarithm of the blood–brain barrier partition (LogBB). The values indicate that newly synthesized molecule would cross blood–brain barrier (BBB) with a low rate. Hence, we checked if this was an issue of other interesting compounds of the series and in particular of **4d**, which also has good inhibitory activity (19.35 ± 0.68 nM). In this case the prediction of CNS activity was positive. Therefore, this compound appears more interesting in this respect. Finally, qualitative human oral absorption was predicted with favourable score. In conclusion, **4d** revealed to have slightly more favorable physicochemical properties and therefore seems to be a good candidate for future development.

3. Conclusion

Given our interest in the development of MAO-B inhibitors as a potential therapeutic strategy for neurodegenerative diseases, we developed molecules with optimized activity toward B isoform. Therefore, we synthesised a new series of 2-(3,4-dichlorophenyl)-3-acetyl-5- aryl-2,3-dihydro-1,3,4-oxadiazoles. The introduction of a second chlorine atom in the 5-phenyl substituent improved potency. Several compounds showed inhibition properties in the nM range and a high selectivity toward MAO-B. As previously observed for similar compounds, the (*R*)-enantiomer exhibits a higher inhibitory activity compared to both the racemic mixture and the (*S*)-enantiomer. We have validated a computational protocol with good qualitative accord between experimental and theoretical activities. Therefore, the devised workflow will be applied for future studies.

4. Experimental

4.1. Chemistry and compounds characterization

4.1.1. General methods

Melting points were uncorrected and were determined on a

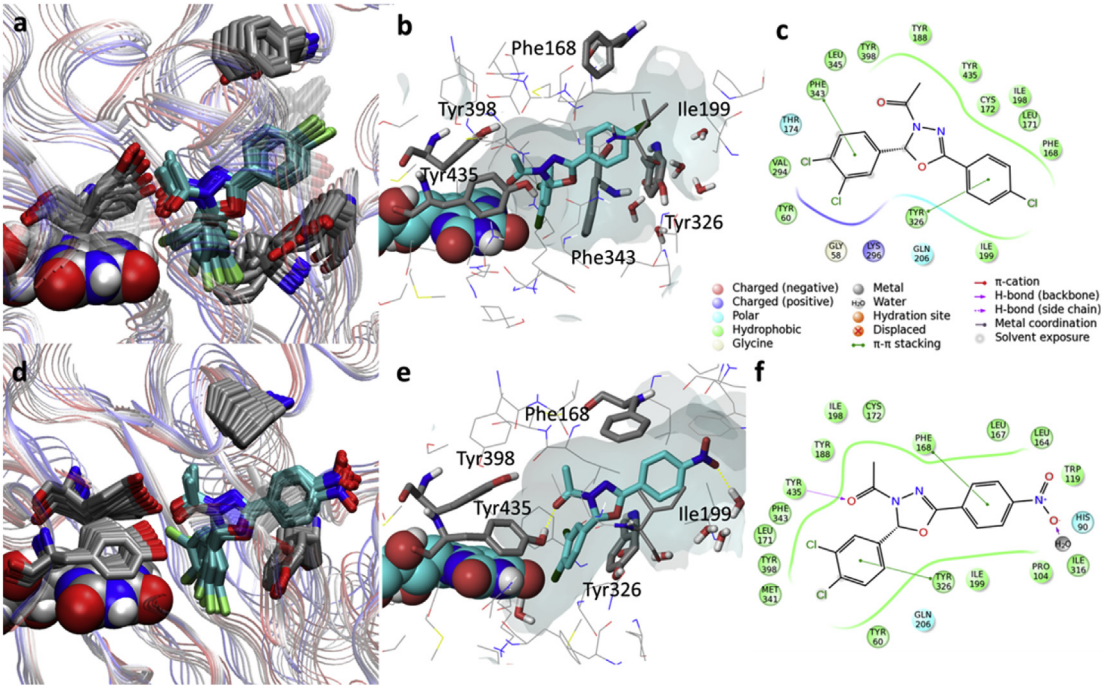

Fig. 6. a) d) Superimposed structures of 10 ns MD simulations frames of [**4e 4f**- MAO-B] complex coloured by time-step: initial (red), final (blue) along with intermediate structures snapshots. b) e) close-up of the binding cavity; c) f) 2D representing compound and interacting residues(For interpretation of the references to colour in this figure legend, the reader is referred to the web version of this article.).

Reichert Kofler thermopan apparatus. ^{1}H NMR spectra were recorded on a Varian Unity 500 and on a Bruker 400, using tetramethylsilane (TMS) as internal standard (chemical shifts in δ values). NMR spectra are reported in Supplementary data. Electron ionisation (EI) mass spectra were obtained by a Fisons QMD 1000 mass spectrometer (70 eV, 200 μA, ion source temperature 200 °C). The samples were introduced directly into the ion source. TLC analyses were performed on silica gel 60 F254 plates. All synthesized compounds were purified by crystallization from an appropriate solvent. Elemental analyses were obtained on a Perkin Elmer 240 B microanalyzer. Analytical data of the synthesised compounds are in agreement within ±0.4% of the theoretical values.

4.1.2. Synthesis of compounds ***4a-j*** *[1]*

Equal amounts of aromatic aldehyde (0.018 mol) and the appropriate arylhydrazide (0.018 mol) were refluxed in ethanol (60 mL) under vigorous stirring from 1 to 3 h in presence of acetic acid as catalyst (0.5 mL). With respect to the different aromatic substituents in positions 2 and 5 of the oxadiazole ring, a differently coloured solution is obtained. The reaction solution is monitored by TLC (eluent dichloromethane: methanol 20:1). After the mixture is cooled at room temperature, the precipitated product is filtered off and then washed with isopropyl ether. Obtained arylidenearylhydrazides (0.003 mol) are refluxed in 6 mL of acetic anhydride under vigorous stirring from 15 min to 2 h. The suspension is monitored by TLC (eluent chloroform: methanol 20:1). The solution is then poured onto ice-water (100 g) and vigorously stirred. A precipitate is formed which is washed with $NaHCO_3$ (10% aqueous solution) to remove the acetic acid. The obtained solid is further purified by crystallization.

4.1.2.1. 4a: 2-(3,4-dichlorophenyl)-3-acetyl-5- pyridin-2,3-dihydro-1,3,4-oxadiazole. $C_{15}H_{11}Cl_2N_3O_2$. Pink powdery solid, M.p. 117–118 °C (isopropyl ether), MS (*m/z*) 294, yield 92%. CHN %: Calc. C, 53.59; H, 3.30; N, 12.50, Found C, 53.55; H, 3.29; N, 12.46.

^{1}H-NMR (500 MHz, DMSO): δ 2.39 (s, 3H), 7.24 (s, 1H), 7.50 (d, 1H, *J* = 8 Hz), 7.73 (m, 3H, *J* = 8, *and* 4 Hz), 7.82 (s, 1H), 8.75 (s, 2H).

^{13}C-NMR (100 MHz, DMSO): δ 21.38, 91.36, 120.39, 127.23, 129.26, 131.39, 131.71, 132.94, 137.15, 150.80 (2C), 153.15, 157.01, 166.44, 166.55.

4.1.2.2. ***4b****: 2-(3,4-dichlorophenyl)-3-acetyl-5- phenyl-2,3-dihydro-1,3,4-oxadiazole.* $C_{16}H_{12}Cl_2N_2O_2$. White crystals, M.p. 99–100 °C (ethanol), MS (*m/z*) 335, yield 43%. CHN %: Calc. C, 57.33; H, 3.61; N, 8.36, Found C, 57.36; H, 3.63; N, 8.37.

^{1}H-NMR (400 MHz, DMSO): δ 2.27 (s, 3H), 7.22 (s, 1H), 7.48 (dd, 1H, *J* = 8.3 *and* 2.0 Hz), 7.54 (t, 2H, *J* = 7.6 Hz), 7.61 (t, 1H, *J* = 7.2 Hz), 7.73 (d, 1H, *J* = 8.4 Hz), 7.95 (d, 1H, *J* = 2 Hz), 7.84 (m, 2H).

^{13}C-NMR (100 MHz, DMSO): δ 21.39, 90.56, 123.89, 126.83 (2C), 127.03, 129.12, 129.32 (2C), 131.46, 131.68, 132.24, 132.79, 137.57, 154.80, 167.27.

4.1.2.3. ***4c****: 2-(3,4-dichlorophenyl)-3-acetyl-5-(4-methoxyphenyl)-2,3-dihydro-1,3,4-oxadiazole.* $C_{17}H_{14}Cl_2N_2O_3$. Pale yellow crystals, M.p. 118–120 °C (ethanol), MS (*m/z*) 364, yield 45%. CHN %: Calc. C, 55.91; H, 3.86; N, 7.67, Found C, 55.89; H, 3.86; N, 7.65.

^{1}H-NMR (500 MHz, DMSO): δ 2.25 (s, 3H), 3.82 (s, 3H), 7.07 (d, 2H, *J* = 9 Hz), 7.17 (1H, s), 7.45 (dd, 1H, *J* = 8.5 and 2.0 Hz), 7.71 (d, 1H, *J* = 8.5 Hz), 7.75 (d, 1H, *J* = 2 Hz), 7.77 (d, 2H, *J* = 8.5 Hz).

^{13}C-NMR (100 MHz, DMSO): δ 21.32, 55.66, 90.16, 114.75 (2C), 115.93, 126.89, 128.69 (2C), 128.99, 131.40, 131.61, 132.67, 137.67, 154.81, 162.29, 167.01.

4.1.2.4. ***4d****: 2-(3,4-dichlorophenyl)-3-acetyl-5-(4-methylphenyl)-2,3-dihydro-1,3,4-oxadiazole.* $C_{17}H_{14}Cl_2N_2O_2$. Pale yellow crystals, M.p. 120–122 °C (isopropyl ether), MS (*m/z*) 348, yield 75%. CHN %: Calc. C, 58.47; H, 4.04; N, 8.02, Found C, 58.50; H, 4.03; N, 8.05.

^{1}H-NMR (400 MHz, DMSO): δ 2.26 (s, 3H), 2.38 (s, 3H), 7.2 (s, 1H), 7.34 (d, 2H, *J* = 8 Hz), 7.46 (dd, 1H, *J* = 8 and 2 Hz), 7.72 (m, 3H,

J = 8, *and* 2 Hz), 7.77 (d, 1H, J = 2 Hz).

^{13}C-NMR (100 MHz, DMSO): δ 21.32, 21.38, 90.37, 121.06, 126.83 (2C), 126.98, 129.07, 129.87 (2C), 130.17, 131.47, 132.76, 137.63, 142.44, 154.94, 167.17.

4.1.2.5. ***4e****: 2-(3,4-dichlorophenyl)-3-acetyl-5-(4-chlorophenyl)-2,3-dihydro-1,3,4-oxadiazole.* $C_{16}H_{11}Cl_3N_2O_2$. Pale yellow crystals, M.p. 119–120 °C (ethanol); MS (*m/z*) 367, yield 92%. CHN %: Calc. C, 51.99; H, 3.00; N, 7.58 Found C, 52.02; H, 3.02; N, 7.60.

^{1}H-NMR (400 MHz, DMSO): δ 2.27 (3H, s), 7.22 (1H, s), 7.48 (1H, dd, J = 8.4 *and* 2.0 Hz), 7.61 (2H, d, J = 8.8 Hz), 7.72 (1H, d, J = 8.4 Hz), 7.80 (1H, d, J = 2.0 Hz), 7.84 (2H, d, J = 8.8 Hz).

^{13}C-NMR (100 MHz, DMSO): δ 21.39, 90.88, 122.83, 127.10, 128.63 (2C), 129.17, 129.49 (2C), 131.44, 131.70, 132.85, 136.88, 137.41, 154.02, 167.34.

4.1.2.6. ***4f****: 2-(3,4-dichlorophenyl)-3-acetyl-5-(4-nitrophenyl)-2,3-dihydro-1,3,4-oxadiazole.* $C_{16}H_{11}Cl_2N_3O_4$. Yellow crystals, M.p. 165–166 °C (ethanol); MS (*m/z*) 348, yield 47%. CHN %: Calc. C, 50.55; H, 2.92; N, 11.05 Found C, 50.53; H, 2.91; N, 11.03.

^{1}H-NMR (500 MHz, DMSO): δ 2.29 (3H, s), 7.26 (1H, s), 7.51 (1H, dd, J = 8 and 1.5 Hz), 7.72 (1H, d, J = 8.5 Hz), 7.83 (1H, d, J = 2.0 Hz), 8.07 (2H, d, J = 8 Hz), 8.35 (2H, d, J = 9 Hz).

^{13}C-NMR (100 MHz, DMSO): δ 21.38, 91.46, 122.51, 124.41 (2C), 127.20, 128.12 (2C), 129.23, 129.83, 131.38, 132.94, 137.14, 149.25, 153.26, 167.55.

4.1.2.7. ***4g****: 2-(3,4-dichlorophenyl)-3-acetyl-5-(4-N,N-dimethylaminophenyl)-2,3-dihydro-1,3,4-oxadiazole.* $C_{18}H_{17}Cl_2N_3O_2$. Yellow crystals, M.p. 156–158 °C (isopropyl ether); MS (*m/z*) 377, yield 76%. CHN %: Calc. C, 57.16; H, 4.53; N, 11.11 Found C, 57.18; H, 4.55; N, 11.13.

^{1}H-NMR (400 MHz, DMSO): δ 2.23 (3H, s), 2.99 (6H, s), 6.77 (2H, d, J = 8.8 Hz), 7.13 (1H, s), 7.43 (1H, dd, J = 8.4, *and* 2 Hz), 7.63 (2H, d, J = 9.2 Hz), 7.72 (2H, m, J = 8.4 Hz).

^{13}C-NMR (100 MHz, DMSO): δ 21.36, 39.80 (2C), 89.55, 109.72, 111.68 (2C), 126.85, 128.20 (2C), 128.94, 131.45, 131.61, 132.58, 137.99, 152.58, 155.69, 166.68.

4.1.2.8. ***4h****: 2-(3,4-dichlorophenyl)-3-acetyl-5-(4-bromophenyl)-2,3-dihydro-1,3,4-oxadiazole.* $C_{16}H_{11}BrCl_2N_2O_2$. White cottony solid, M.p. 140–142 °C (ethanol); MS (*m/z*) 411, yield 47%. CHN %: Calc. C, 46.41; H, 2.68; N, 6.77 Found C, 46.40; H, 2.69; N, 6.78.

^{1}H-NMR (400 MHz, DMSO): δ 2.27 (3H, s), 7.22 (1H, s), 7.48 (1H, dd, J = 8.4 and 2.0 Hz), 7.72 (1H, d, J = 8.4 Hz), 7.76 (4H, m, J = 2.0 Hz), 7.79 (1H, d, J = 2 Hz).

^{13}C-NMR (100 MHz, DMSO): δ 21.39, 90.88, 123.17, 125.77, 127.10, 128.74 (2C), 129.17, 131.44, 131.70, 132.41 (2C), 132.85, 137.40, 154.13, 167.34.

4.1.2.9. ***4i****: 2-(3,4-dichlorophenyl)-3-acetyl-5-(4-cyanophenyl)-2,3-dihydro-1,3,4-oxadiazole.* $C_{17}H_{11}Cl_2N_3O_2$. Pale yellow crystals, M.p. 148–150 °C (ethanol/isopropanol); MS (*m/z*) 359, yield 86%. CHN %: Calc. C, 56.69; H, 3.08; N, 11.67; N, 6.77 Found C, 56.68; H, 3.09, N, 11.68.

^{1}H-NMR (400 MHz, DMSO): δ 2.28 (3H, s), 7.25 (1H, s); 7.50 (1H, dd, J = 8.4, *and* 2.0 Hz); 7.72 (1H, d, J = 8 Hz), 7.83 (1H, d, J = 2.0 Hz), 7.99 (4H, m, J = 8.6 Hz).

^{13}C-NMR (100 MHz, DMSO): δ 21.39, 91.34, 114.13, 118.30, 127.22, 127.48 (2C), 128.23, 128.72, 129.25, 131.41, 131.73, 133.21 (2C), 137.22, 153.51, 167.54.

4.1.2.10. ***4j****: 2-(3,4-dichlorophenyl)-3-acetyl-5-(2-methylphenyl)-2,3-dihydro-1,3,4-oxadiazole.* $C_{17}H_{14}Cl_2N_2O_2$. White solid, M.p. 147–150 °C (hexane); MS (*m/z*) 348, yield 32%. CHN %: Calc. C, 58.47; H, 4.04; N, 8.02 Found C,58.49; H, 4.06; N, 8.04.

^{1}H-NMR (400 MHz, DMSO): δ 2.43 (3H, s), 2.70 (3H, s), 7.45 (1H, s), 7.54 (1H, t, CH, J = 7.33 Hz), 7.78 (1H, d, J = 7.6 Hz), 7.88 (1H, dd, J = 8.2 and 2.2), 8.09 (1H, td, J = 7.6 *and* 1.5 Hz), 8.14 (3H, m).

^{13}C-NMR (100 MHz, DMSO): δ 20.18, 23.11, 91.37, 126.39, 128.28, 128.39, 128.56, 128.95, 129.71, 130.58, 131.34, 132.12, 132.98, 133.35, 136.50, 154.70, 157.99.

4.1.3. HPLC resolution of ***4d-f***

The enantioseparations of **4d-f** were performed by using the stainless-steel Chiralpak IA (250 mm × 4.6 mm i.d. and 250 × 10 mm i.d.) (Chiral Technologies Europe, Illkirch, France) columns. All chemicals and solvents for HPLC were purchased from Aldrich (Italy) and used without further purification. The analytical HPLC apparatus consisted of a Perkin–Elmer (Norwalk, CT, USA) 200 lc pump equipped with a Rheodyne (Cotati, CA, USA) injector, a 20-μl sample loop, a HPLC Dionex CC-100 oven (Sunnyvale, CA, USA) and a Jasco (Jasco, Tokyo, Japan) Model CD 2095 Plus UV/CD detector. For semipreparative separations a Perkin–Elmer 200 LC pump equipped with a Rheodyne injector, a 1 mL sample loop, a Perkin–Elmer LC 101 oven and Waters 484 detector (Waters Corporation, Milford, MA, USA) were used. The signal was acquired and processed by Clarity software (DataApex, Prague, The Czech Republic).

4.1.4. Circular dichroism

The CD spectra were measured in ethanol solution by using a Jasco Model J-700 spectropolarimeter. The concentration was 0.2 mg/mL. The optical path and temperature were set at 0.1 mm and 20 °C, respectively. The spectra were average computed over three instrumental scans and the intensities were presented in terms of ellipticity values (mdeg).

4.1.5. Polarimetry

Specific rotations were measured at 589 nm by a PerkinElmer polarimeter model 241 equipped with a Na/Hg lamp. The volume of the cell was 1 cm^3 and the optical path was 10 cm. The system was set at 20 °C.

4.1.6. Crystal structure determination for compound ***4d***

$C_{17}H_{14}Cl_2N_2O_2$ M = 349.21, Monoclinic, space group P 21, a = 9.095(1), b = 6.552(1), c = 13.870(1)Å, β = 95.982(4), V = 822.0(2)Å3, Z = 2 Dc = 1.415, μ = 3.643 mm-1, F(000) = 362. 3040 reflections were collected with a 4.89<θ < 69.78 range with a completeness to theta 95.7%; 2307 were unique, the parameters were 213 and the final R index was 0.0446 for reflections having I > 2σI and 0.0689 for all data. A colourless prismatic shaped crystal (0.08 × 0.06 × 0.02) was used for data collection. Hydrogen atoms were assigned in calculated positions, except H2 (on asymmetric C2) which was found in the F.D map. RX-analysis was carried out with a Goniometer Oxford Diffraction KM4 Xcalibur2 at room temperature. Cu/Kα radiation (40 mA/-40 KV), monochromated by an Oxford Diffraction Enhance ULTRA assembly, and an Oxford Diffraction Excalibur PX Ultra CCD were used for cells parameters determination and data collection. The integrated intensities, measured using the ω scan mode, were corrected for Lorentz and polarization effects [53]. Direct methods of SIR2004 [54] were used in solving the structures and they were refined using the full-matrix least squares on F2 provided by SHELXL97 [55]. Multi-scan symmetry-related measurement was used as experimental absorption correction type. The non-hydrogen atoms were refined anisotropically whereas hydrogen atoms were refined as isotropic. The X-ray CIF file for this structure has been deposited at the Cambridge Crystallographic Data Centre and allocated with the deposition number CCDC 1030508. Copies of the data can be

obtained, free of charge, from CCDC, 12 Union Road, Cambridge, CB2 1EZ UK (e-mail: deposit@ccdc.cam.ac.uk; http://www.ccdc.cam.ac.uk).

4.2. Enzymatic assay

MAO inhibition measurements were evaluated following the general procedure previously described by us [42]. Briefly, test drugs and adequate amounts of recombinant hMAO-A or hMAO-B (Sigma–Aldrich Quiímica S.A., Alcobendas, Spain) required and adjusted to oxidize 165 pmol of *p*-tyramine/min in the control group, were incubated for 15 min at 37 °C in a flat-black-bottom 96-well microtest plate (BD Biosciences, Franklin Lakes, NJ) placed in the dark fluorimeter chamber. The reaction was started by adding 200 μM Amplex Red reagent (Molecular Probes, Inc., Eugene, OR), 1 U/mL horseradish peroxidase, and 1 mM p-tyramine and the production of resorufin, was quantified at 37 °C in a multidetection microplate fluorescence reader (FLX800, Bio-Tek Instruments, Inc., Winooski, VT) based on the fluorescence generated (excitation, 545 nm; emission, 590 nm). The specific fluorescence emission was calculated after subtraction of the background activity, which was determined from vials containing all components except the hMAO isoforms, which were replaced by a sodium phosphate buffer solution.

4.3. Molecular modelling

4.3.1. MAO-B active site characterization

The previous reported[1] theoretical complex between the PDB MAO-B and the most active compound 2-(4-chlorophenyl)-3-acetyl-5-(4-chlorophenyl)-2,3-dihydro-1,3,4-oxadiazole was considered for the active site characterization. The binding cleft was defined by means of a regular box of 1000 $Å^3$ centred onto the ligand position. After removing the inhibitor, GRID [41] software was applied for mapping the target previous defined using CL, BR, AR.COO^-, C3 and ON probes for mimicking organic chlorine and bromine atoms, aromatic carboxylic moiety, methyl and nitro group oxygen respectively. Default software directives were taken into account except for the number of planes per Angstrom (NPLA) that was increased till 3 corresponding to a grid spacing equal to 0.333 Å. Computed isocontour maps were displayed using VMD ver. 1.9.1 [56] and graphical inspected considering an energy threshold equal to −5.5 kcal/mol for all probes except C3 whose maps were analyzed at −3.5 kcal/mol.

4.3.2. Docking protocol

Three-dimensional coordinates of the receptor [7] were obtained from the Protein Data Bank (PDB). The protein was processed and the internal hydrogen bonding network of the receptor was optimized using the algorithm implemented in Protein Preparation wizard [57]. In order to compare energetic analysis it has been necessary complete the transmembrane portion considering the aminoacid sequence and α–helix packing reported in literature [58,59]. The mitochondrial bilayer membrane was simulated with an Dipalmitoylphosphatidylcholine (DPPC) bilayer [60]. Three-dimensional ligand structures for all docking experiments were built using Maestro GUI. Structures were optimized by means of energy minimization carried out using the Merck Molecular Force Field (MMFFs) [61], the Generalized Born/Surface Area (GB/SA) [62] water implicit solvation model and the Polak–Ribier Coniugate Gradient (PRCG) method, converging on gradient with a threshold of 0.05 kJ $(molÅ)^{-1}$ as implemented in Macromodel. Molecular docking studies were performed using Glide SP [46], Glide XP [63], QMPL [47,48] and Induced Fit workflow protocol [64]. Grids were defined around the refined structure by centring on co-crystallized ligand reported into the PDB entry 2V5Z [7].

4.3.3. Molecular dynamics

The docking resulting complexes were solvated with a box of TIP3P (Transferable Intermolecular Potential 3-Point) water [65] and counter ions were added creating an overall neutral system simulating approximately 0.15 M NaCl. The ions were equally distributed in a water box. The final system was subjected to a MD simulation up to 10 ns using Desmond [66]. Restraint force of 50 kcal/(mol·Å) was added to monomer and dimer transmembrane portion whereas the dimer in membrane was left without any restraint. The solvated models were optimized, and subsequently the MTK_NPT (Martyna-Tobias-Klein with constant Number of particles, Pressure and Temperature) ensemble was employed [67]. The default stages in the relaxation process for the NPT ensemble included two energy minimizations and four simulation steps. During the energy minimizations, two runs of 2000 iteration were processed using the steepest descent method: during the first run, the protein structure was fixed by a force restraint constant of 50 kcal/(mol·Å) and in the second all restraints were removed. With the first simulation, at NVT (constant Number of particles, Volume, and Temperature) ensemble, the system reached a temperature of 10 K. In the following three simulations in the NPT ensemble, the system was heated up to 325 K and the pressure was kept constant at 1 bar using the Berendsen thermostat–barostat. During the production phase, temperature and pressure were kept constant using the Nosè-Hoover thermostat–barostat. The energy and trajectory were recorded every 1.2 ps and 4.8 ps, respectively. For multiple time step integration, RESPA (REversible reference System Propagator Algorithm) [68] was applied to integrate the equation of motion with Fourier-space electrostatics computed every 6 fs, and all remaining interactions computed every 2 fs. All chemical bond lengths involving hydrogen atoms were fixed with SHAKE [69]. Short range cut-off was set to 9 Å and the smooth particle mesh Ewald method (PME) [70] were used for long range electrostatic interaction. The MD trajectories were analyzed in terms of interaction energies and geometries.

4.3.4. ADME-tox prediction

The energy minimized ligands structures were evaluated for their drug-like properties using Qikprop [52] which predicts physically significant descriptors and pharmaceutically relevant properties of organic molecules [71,72]. Results are reported in Table S3.

Acknowledgment

The authors wish to acknowledge Fondazione Banco di Sardegna for financial support.

Appendix A. Supplementary data

Supplementary data related to this article can be found at http://dx.doi.org/10.1016/j.ejmech.2015.12.026.

References

[1] E. Maccioni, S. Alcaro, R. Cirilli, S. Vigo, M.C. Cardia, M.L. Sanna, R. Meleddu, M. Yanez, G. Costa, L. Casu, P. Matyus, S. Distinto, 3-Acetyl-2,5-diaryl-2,3-dihydro-1,3,4-oxadiazoles: a new scaffold for the selective inhibition of monoamine oxidase B, J. Med. Chem. 54 (2011) 6394–6398.
[2] C. Binda, E.M. Milczek, D. Bonivento, J. Wang, A. Mattevi, D.E. Edmondson, Lights and shadows on monoamine oxidase inhibition in neuroprotective pharmacological therapies, Curr. Top. Med. Chem. 11 (2011) 2788–2796.
[3] S.K. Amit, C. Neal, T. Bernard, Selective inhibitors of monoamine oxidase (MAO-A and MAO-B) as probes of its catalytic site and mechanism, Med. Res. Rev. 15 (1995) 325–388.

[4] D.E. Edmondson, C. Binda, A. Mattevi, Structural insights into the mechanism of amine oxidation by monoamine oxidases A and B, Arch. Biochem. Biophys. 464 (2007) 269–276.
[5] R.G. Fariello, Safinamide, Neurotherapeutics 4 (2007) 110–116.
[6] T. Müller, Current status of safinamide for the drug portfolio of Parkinson's disease therapy, Expert Rev. Neurother. 13 (2013) 969–977.
[7] C. Binda, J. Wang, L. Pisani, C. Caccia, A. Carotti, P. Salvati, D.E. Edmondson, A. Mattevi, Structures of human monoamine oxidase B complexes with selective noncovalent inhibitors: safinamide and coumarin analogs, J. Med. Chem. 50 (2007) 5848–5852.
[8] F. Hubálek, C. Binda, A. Khalil, M. Li, A. Mattevi, N. Castagnoli, D.E. Edmondson, Demonstration of isoleucine 199 as a structural determinant for the selective inhibition of human monoamine oxidase B by specific reversible inhibitors, J. Biol. Chem. 280 (2005) 15761–15766.
[9] J.-F. Chen, S. Steyn, R. Staal, J.P. Petzer, K. Xu, C.J. Van der Schyf, K. Castagnoli, P.K. Sonsalla, N. Castagnoli, M.A. Schwarzschild, 8-(3-Chlorostyryl)caffeine may attenuate MPTP neurotoxicity through dual actions of monoamine oxidase inhibition and A2A receptor antagonism, J. Biol. Chem. 277 (2002) 36040–36044.
[10] J. Petzer, N. Castagnoli, M. Schwarzschild, J.-F. Chen, C. Schyf, Dual-target-directed drugs that block monoamine oxidase B and adenosine A2A receptors for Parkinson's disease, Neurotherapeutics 6 (2009) 141–151.
[11] C. Binda, M. Aldeco, W.J. Geldenhuys, M. Tortorici, A. Mattevi, D.E. Edmondson, Molecular insights into human monoamine oxidase B inhibition by the glitazone antidiabetes drugs, ACS Med. Chem. Lett. 3 (2011) 39–42.
[12] H.P. Volz, C.H. Gleiter, Monoamine oxidase inhibitors. A perspective on their use in the elderly, Drugs Aging 13 (1998) 341–355.
[13] G.G.S. Collins, M. Sandler, E.D. Williams, M.B.H. Youdim, Multiple forms of human brain mitochondrial monoamine oxidase, Nature 225 (1970) 817–820.
[14] A.-M. O'Carroll, C. Fowler, J. Phillips, I. Tobbia, K. Tipton, The deamination of dopamine by human brain monoamine oxidase, Schmiedeb. Arch. Pharmacol. 322 (1983) 198–202.
[15] M.B.H. Youdim, D. Edmondson, K.F. Tipton, The therapeutic potential of monoamine oxidase inhibitors, Nat. Rev. Neurosci. 7 (2006) 295–309.
[16] W.G. Tatton, W.Y.L. Ju, D.P. Holland, C. Tai, M. Kwan, (−)-Deprenyl reduces PC12 cell apoptosis by inducing new protein synthesis, J. Neurochem. 63 (1994) 1572–1575.
[17] S. Mínguez-Mínguez, J. Solís-García del Pozo, J. Jordán, Rasagiline in Parkinson's disease: a review based on meta-analysis of clinical data, Pharmacol. Res. 74 (2013) 78–86.
[18] M. Unzeta, E. Sanz, Novel MAO-B inhibitors: potential therapeutic use of the selective MAO-B inhibitor PF9601N in Parkinson's Disease, in: B.H.Y. Moussa, D. Peter (Eds.), International Review of Neurobiology, Academic Press, 2011, pp. 217–236.
[19] J. Saura, J.M. Luque, A.M. Cesura, M. Da Prada, V. Chan-Palay, G. Huber, J. Loffler, J.G. Richards, Increased monoamine oxidase B activity in plaque-associated astrocytes of Alzheimer brains revealed by quantitative enzyme radioautography, Neuroscience 62 (1994) 15–30.
[20] M. Sano, C. Ernesto, R.G. Thomas, M.R. Klauber, K. Schafer, M. Grundman, P. Woodbury, J. Growdon, C.W. Cotman, E. Pfeiffer, L.S. Schneider, L.J. Thal, A controlled trial of selegiline, alpha-tocopherol, or both as treatment for Alzheimer's disease, N. Engl. J. Med. 336 (1997) 1216–1222.
[21] O. Weinreb, T. Amit, O. Bar-Am, M.B.H. Youdim, A novel anti-Alzheimer's disease drug, Ladostigil: neuroprotective, multimodal brain-selective monoamine oxidase and cholinesterase inhibitor, in: B.H.Y. Moussa, D. Peter (Eds.), International Review of Neurobiology, Academic Press, 2011, pp. 191–215.
[22] H. Zheng, S. Gal, L.M. Weiner, O. Bar-Am, A. Warshawsky, M. Fridkin, M.B.H. Youdim, Novel multifunctional neuroprotective iron chelator-monoamine oxidase inhibitor drugs for neurodegenerative diseases: In vitro studies on antioxidant activity, prevention of lipid peroxide formation and monoamine oxidase inhibition, J. Neurochem. 95 (2005) 68–78.
[23] A. Nicotra, F. Pierucci, H. Parvez, O. Senatori, Monoamine oxidase expression during development and aging, Neurotoxicology 25 (2004) 155–165.
[24] M.J. Kumar, J. Andersen, Perspectives on MAO-B in aging and neurological disease, Mol. Neurobiol. 30 (2004) 77–89.
[25] A.M. Palmer, S.T. DeKosky, Monoamine neurons in aging and Alzheimer's disease, J. Neural. Transm. Gen. Sect. 91 (1993) 135–159.
[26] G. Alper, F.K. Girgin, M. Ozgönül, G. Menteş, B. Ersöz, MAO inhibitors and oxidant stress in aging brain tissue, Eur. Neuropsychopharmacol. 9 (1999) 247–252.
[27] P.F. Good, P. Werner, A. Hsu, C.W. Olanow, D.P. Perl, Evidence for neuronal oxidative damage in Alzheimer's disease, Am. J. Pathol. 149 (1996) 21–28.
[28] J.K. Mallajosyula, D. Kaur, S.J. Chinta, S. Rajagopalan, A. Rane, D.G. Nicholls, D.A. Di Monte, H. Macarthur, J.K. Andersen, MAO-B elevation in mouse brain astrocytes results in Parkinson's pathology, PLoS One 3 (2008) e1616.
[29] S. Fahn, G. Cohen, The oxidant stress hypothesis in Parkinson's disease: Evidence supporting it, Ann. Neurol. 32 (1992) 804–812.
[30] W.K. Wong, X.-M. Out, K. Chen, J.C. Shih, Activation of human monoamine oxidase B gene expression by a protein kinase C MAPK signal transduction pathway involves c-Jun and Egr-1, J. Biol. Chem. 277 (2002) 22222–22230.
[31] J.Y. Chung, J.W. Lee, C.H. Ryu, H.K. Min, Y.J. Yoon, M.J. Lim, C.H. Park, 1-[2-(4-Benzyloxyphenoxy)ethyl]imidazole inhibits monoamine oxidase B and protects against neuronal loss and behavioral impairment in rodent models of Parkinson's disease, J. Neurosci. Res. 93 (2015) 1267–1278.
[32] A.D. Cash, G. Perry, M.A. Smith, Therapeutic potential in alzheimer disease, Curr. Med. Chem. 9 (2002) 1605–1610.
[33] P.H. Yu, Pharmacological and clinical implications of MAO-B inhibitors, Gen. Pharmacol. Vasc. S. 25 (1994) 1527–1539.
[34] Z.-X. Pan, X. He, Y.-Y. Chen, W.-J. Tang, J.-B. Shi, Y.-L. Tang, B.-A. Song, J. Li, X.-H. Liu, New 2H-chromene-3-carboxamide derivatives: design, synthesis and use as inhibitors of hMAO, Eur. J. Med. Chem. 80 (2014) 278–284.
[35] L. Pisani, R. Farina, O. Nicolotti, D. Gadaleta, R. Soto-Otero, M. Catto, M. Di Braccio, E. Mendez-Alvarez, A. Carotti, In silico design of novel 2H-chromen-2-one derivatives as potent and selective MAO-B inhibitors, Eur. J. Med. Chem. 89 (2015) 98–105.
[36] D. Secci, A. Bolasco, S. Carradori, M. D'Ascenzio, R. Nescatelli, M. Yáñez, Recent advances in the development of selective human MAO-B inhibitors: (Hetero) arylidene-(4-substituted-thiazol-2-yl)hydrazines, Eur. J. Med. Chem. 58 (2012) 405–417.
[37] S.-S. Xie, X. Wang, N. Jiang, W. Yu, K.D.G. Wang, J.-S. Lan, Z.-R. Li, L.-Y. Kong, Multi-target tacrine-coumarin hybrids: cholinesterase and monoamine oxidase B inhibition properties against Alzheimer's disease, Eur. J. Med. Chem. 95 (2015) 153–165.
[38] F. Chimenti, E. Maccioni, D. Secci, A. Bolasco, P. Chimenti, A. Granese, O. Befani, P. Turini, S. Alcaro, F. Ortuso, R. Cirilli, F. La Torre, M.C. Cardia, S. Distinto, Synthesis, molecular modeling studies, and selective inhibitory activity against monoamine oxidase of 1-thiocarbamoyl-3,5-diaryl-4,5-dihydro-(1H)-pyrazole derivatives, J. Med. Chem. 48 (2005) 7113–7122.
[39] F. Chimenti, E. Maccioni, D. Secci, A. Bolasco, P. Chimenti, A. Granese, O. Befani, P. Turini, S. Alcaro, F. Ortuso, M.C. Cardia, S. Distinto, Selective inhibitory activity against MAO and molecular modeling studies of 2-thiazolylhydrazone derivatives, J. Med. Chem. 50 (2007) 707–712.
[40] F. Chimenti, D. Secci, A. Bolasco, P. Chimenti, A. Granese, S. Carradori, E. MacCioni, M.C. Cardia, M. Yáñez, F. Orallo, S. Alcaro, F. Ortuso, R. Cirilli, R. Ferretti, S. Distinto, J. Kirchmair, T. Langer, Synthesis, semipreparative HPLC separation, biological evaluation, and 3D-QSAR of hydrazothiazole derivatives as human monoamine oxidase B inhibitors, Bioorg. Med. Chem. 18 (2010) 5063–5070.
[41] P.J. Goodford, A computational procedure for determining energetically favorable binding sites on biologically important macromolecules, J. Med. Chem. 28 (1985) 849–857.
[42] S. Distinto, M. Yáñez, S. Alcaro, M.C. Cardia, M. Gaspari, M.L. Sanna, R. Meleddu, F. Ortuso, J. Kirchmair, P. Markt, A. Bolasco, G. Wolber, D. Secci, E. MacCioni, Synthesis and biological assessment of novel 2-thiazolylhydrazones and computational analysis of their recognition by monoamine oxidase B, Eur. J. Med. Chem. 48 (2012) 284–295.
[43] R.Z. Cer, U. Mudunuri, R. Stephens, F.J. Lebeda, IC50-to-K-i: a web-based tool for converting IC50 to K-i values for inhibitors of enzyme activity and ligand binding, Nucleic Acids Res. 37 (2009) W441–W445.
[44] G. Cerioni, E. Maccioni, M.C. Cardia, S. Vigo, F. Mocci, Characterization of 2,5-diaryl-1,3,4-oxadiazolines by multinuclear magnetic resonance and density functional theory calculations. investigation on a case of very remote hammett correlation, Magn. Reson. Chem. 47 (2009) 727–733.
[45] H.M. Berman, J. Westbrook, Z. Feng, G. Gilliland, T.N. Bhat, H. Weissig, I.N. Shindyalov, P.E. Bourne, The protein data bank, Nucleic Acids Res. 28 (2000) 235–242.
[46] R.A. Friesner, J.L. Banks, R.B. Murphy, T.A. Halgren, J.J. Klicic, D.T. Mainz, M.P. Repasky, E.H. Knoll, M. Shelley, J.K. Perry, D.E. Shaw, P. Francis, P.S. Shenkin, Glide: A new approach for rapid, accurate docking and scoring. 1. Method and assessment of docking accuracy, J. Med. Chem. 47 (2004) 1739–1749.
[47] F. Mohamadi, N.G.J. Richards, W.C. Guida, R. Liskamp, M. Lipton, C. Caufield, G. Chang, T. Hendrickson, W.C. Still, Macromodel—an integrated software system for modeling organic and bioorganic molecules using molecular mechanics, J. Comput. Chem. 11 (1990) 440–467.
[48] J.Y. Chung, J.-M. Hah, A.E. Cho, Correlation between performance of QM/MM docking and simple classification of binding sites, J. Chem. Inf. Model 49 (2009) 2382–2387.
[49] G.L. Warren, C.W. Andrews, A.-M. Capelli, B. Clarke, J. LaLonde, M.H. Lambert, M. Lindvall, N. Nevins, S.F. Semus, S. Senger, G. Tedesco, I.D. Wall, J.M. Woolven, C.E. Peishoff, M.S. Head, A critical assessment of docking programs and scoring functions, J. Med. Chem. 49 (2006) 5912–5931.
[50] D.E. Edmondson, C. Binda, J. Wang, A.K. Upadhyay, A. Mattevi, Molecular and mechanistic properties of the membrane-bound mitochondrial monoamine oxidases, Biochemistry 48 (2009) 4220–4230.
[51] D. Lagorce, C. Reynes, A.-C. Camproux, M.A. Miteva, O. Sperandio, B.O. Villoutreix, In silico ADME/Tox predictions, in: ADMET for Medicinal Chemists, John Wiley & Sons, Inc, 2011, pp. 29–124.
[52] Qikprop, in: Schrodinger Suite, Schrödinger LLC., New York, NY, USA.
[53] N. Walker, D. Stuart, An empirical method for correcting diffractometer data for absorption effects, Acta Crystallogr. Sect. A 39 (1983) 158–166.
[54] M.C. Burla, R. Caliandro, M. Camalli, B. Carrozzini, G.L. Cascarano, L. De Caro, C. Giacovazzo, G. Polidori, R. Spagna, SIR2004: an improved tool for crystal structure determination and refinement, J. Appl. Crystallogr. 38 (2005) 381–388.
[55] G.M. Sheldrick, SHELXL97: program for crystal structure refinement, Institut für Anorganische Chemie de Universitat Göttingen, 1997.
[56] W. Humphrey, A. Dalke, K. Schulten, VMD: Visual molecular dynamics, J. Mol. Graph 14 (1996) 33–38.

[57] D. Piomelli, O. Sasso, Peripheral gating of pain signals by endogenous lipid mediators, Nat. Neurosci. 17 (2014) 164–174.
[58] C. Binda, F. Hubálek, M. Li, D.E. Edmondson, A. Mattevi, Crystal structure of human monoamine oxidase B, a drug target enzyme monotopically inserted into the mitochondrial outer membrane, FEBS Lett. 564 (2004) 225–228.
[59] J. Ma, M. Yoshimura, E. Yamashita, A. Nakagawa, A. Ito, T. Tsukihara, Structure of rat monoamine oxidase A and its specific recognitions for substrates and inhibitors, J. Mol. Biol. 338 (2004) 103–114.
[60] K. Balali-Mood, P.J. Bond, M.S.P. Sansom, Interaction of monotopic membrane enzymes with a lipid bilayer: a coarse-grained MD simulation study, Biochemistry 48 (2009) 2135–2145.
[61] T. Halgren, Merck molecular force field. II. MMFF94 van der Waals and electrostatic parameters for intermolecular interactions, J. Comput. Chem. 17 (1996) 520–552.
[62] W. Hasel, T.F. Hendrickson, W.C. Still, A rapid approximation to the solvent accessible surface areas of atoms, Tetrahedron comput. Methodol. 1 (1988) 103–116.
[63] R.A. Friesner, R.B. Murphy, M.P. Repasky, L.L. Frye, J.R. Greenwood, T.A. Halgren, P.C. Sanschagrin, D.T. Mainz, Extra precision glide: Docking and scoring incorporating a model of hydrophobic enclosure for protein–ligand complexes, J. Med. Chem. 49 (2006) 6177–6196.
[64] W. Sherman, T. Day, M.P. Jacobson, R.A. Friesner, R. Farid, Novel procedure for modeling ligand/receptor induced fit effects, J. Med. Chem. 49 (2005) 534–553.
[65] W.L. Jorgensen, J. Chandrasekhar, J.D. Madura, R.W. Impey, M.L. Klein, Comparison of simple potential functions for simulating liquid water, J. Chem. Phys. 79 (1983) 926–935.
[66] K.J. Bowers, R.O. Dror, D.E. Shaw, The midpoint method for parallelization of particle simulations, J. Chem. Phys. 124 (2006) 184109–184111.
[67] G.J. Martyna, D.J. Tobias, M.L. Klein, Constant pressure molecular dynamics algorithms, J. Chem. Phys. 101 (1994) 4177–4189.
[68] D.A. Gibson, E.A. Carter, Time-reversible multiple time-scale ab-initio molecular-dynamics, J. Phys. Chem. 97 (1993) 13429–13434.
[69] J.-P. Ryckaert, G. Ciccotti, H. Berendsen, Numerical integration of the cartesian equations of motion of a system with constraints: molecular dynamics of N-alkanes, J. Comput. Phys. 23 (1977) 327–341.
[70] T. Darden, D. York, L. Pedersen, Particle mesh Ewald: an N [center-dot] log(N) method for Ewald sums in large systems, J. Chem. Phys. 98 (1993) 10089–10092.
[71] C.A. Lipinski, F. Lombardo, B.W. Dominy, P.J. Feeney, Experimental and computational approaches to estimate solubility and permeability in drug discovery and development settings, Adv. Drug Deliv. Rev. 46 (2001) 3–26.
[72] W.L. Jorgensen, E.M. Duffy, Prediction of drug solubility from structure, Adv. Drug Deliv. Rev. 54 (2002) 355–366.